JOURNAL OF APPLIED PHYSICS **97**, 074311 (2005)

Nanomechanical characterization of cavity growth and rupture in hydrogen-implanted single-crystal $BaTiO_3$

Young-Bae Park[a)]
Thomas J. Watson Laboratory of Applied Physics, California Institute of Technology, Pasadena, California 91125

Patrick Nardi and Xiaodong Li[b)]
Department of Mechanical Engineering, University of South Carolina, 300 Main Street, Columbia, South Carolina 29208

Harry A. Atwater
Thomas J. Watson Laboratory of Applied Physics, California Institute of Technology, Pasadena, California 91125

(Received 28 September 2004; accepted 15 February 2005; published online 25 March 2005)

A thermodynamic model of cavity nucleation and growth in ion-implanted single-crystal $BaTiO_3$ layer is proposed, and cavity formation is related to the measured mechanical properties to better understand hydrogen implantation-induced layer transfer processes for ferroelectric thin films. The critical radius for cavity nucleation was determined experimentally from blistering experiments performed under isochronal anneal conditions and was calculated using continuum mechanical models for deformation and fracture, together with thermodynamic models. Based on thermodynamic modeling, we suggest that cavities grow toward the cracking criteria at a critical blister size whereupon gas is emitted from ruptured cavities. The main driving force for layer splitting is the reduction of the overall elastic energy stored in the implanted region during the cavity nucleation and growth as the gaseous H_2 entrapped within the cavities is released. Nanoindentation measurements reveal locally the mechanical property changes within the vicinity of a single cavity. Using the measured mechanical properties at the single-cavity level, we developed three-dimensional strain and stress profiles using finite element method. © *2005 American Institute of Physics*. [DOI: 10.1063/1.1885183]

I. INTRODUCTION

Ferroelectric materials have been extensively investigated in many scientific and technological applications because of their physical properties (electrostriction, electro-optical, and nonlinear optical properties), which are related to the development of spontaneous polarization below the Curie temperature. During the last several decades, thin-film ferroelectric materials have been widely used for applications in capacitors and gate dielectrics for nonvolatile random access memory (NVRAM) devices, actuators and microfluidic pumps in microelectromechanical system (MEMS), and electro-optical modulators.[1–3] In most of these cases, ferroelectric thin films have had a polycrystalline microstructure which may affect domain switching, charge retention, and time-dependent fatigue, as well as the magnitude of the macroscopic polarization and piezoelectric coefficients. Thus it has long been desirable, but not generally possible, to obtain truly single-crystal ferroelectric thin films on arbitrary substrates. Recently developed wafer bonding and layer transfer methods have promised to enable the goal of fabricating single-crystal films on substrates of choice. Hence this paper examines the evolution of mechanical properties of ferroelectric materials during the initial stages of the layer transfer process.

In order to obtain single-crystal films, ion-implantation-induced layer transfer techniques similar to the one reported by Bruel in 1995 are among the most viable methods for fabrication that maintains the desirable properties of the parent single-crystal material, and also circumvents the lattice mismatch problems associated with epitaxial growth.[4] Ion-implantation-induced layer transfer processes have been reported for the layer transfer of silicon, InP, GaAs, Ge, and diamond.[5–7] Recently, layer splitting and transfer of the ferroelectric materials and other crystalline perovskite oxide materials such as $LiNbO_3$, $LiAlO_3$, $KTaO_3$, $SrTiO_3$, and $BaTiO_3$ also have been reported, using wet etching and anodic bonding combined with ion-implantation-induced layer transfer methods.[8–14] Szafraniak *et al.* reported that microbubbles were formed at the ion projected range as a result of high-dose hydrogen implantation.[13] They also showed that the transferred ferroelectric thin films retain single-crystal properties of good crystallinity and ferroelectricity.[13,14]

However, to date, the cavity-growth mechanisms operative during layer splitting of ferroelectric materials and the mechanistic role of hydrogen during thermal annealing have not been reported at the level of detail as has been reported for silicon. Furthermore, the chemical and structural effects of implanted gas (hydrogen or helium) in ferroelectric mate-

[a)]Author to whom correspondence should be sent; electronic mail: ypark@caltech.edu
[b)]Electronic mail: lixiao@engr.sc.edu

rials on the piezoelectric and ferroelectric properties of the transferred thin films are still unknown. In addition, to date, there are no detailed reports on the changes in mechanical properties of ion-implanted ferroelectric materials. In general, ion implantation processes alter the mechanical properties and microstructure of crystalline solids by defect formation via atomic displacements and secondary damage evolution, such as dislocation formation, point defect complex formation, precipitation, and phase transformation from the crystalline to the amorphous state. The phase transformation in ferroelectric thin-film materials can, in turn, induce local strain (stress) and hence change mechanical properties. Nanoindentation is a useful technique to measure the mechanical properties of solid surfaces and thin films, such as Young's modulus, hardness, and fracture toughness at a very local level.[15–17]

In this study, we performed H^+ and He^+ implantation in single-crystal $BaTiO_3$, followed by isochronal annealing to investigate the initial stages of cavity nucleation and growth, with modeling using the classical nucleation theory. We measured the local mechanical property changes using nanoindentation techniques, measuring the mechanical deformation of the ferroelectric thin layer during the cavity nucleation and growth. Finally, we developed quantitative stress and strain distributions at the level of an individual cavity using the finite element analysis.

II. EXPERIMENT

For ion-implantation-induced layer transfer, ion implantation was performed with H^+ implantation and/or H^+ and He^+ implantation in bulk single-crystal $BaTiO_3$ substrates (double side polished, (001)-orientation, $5\times5\times1$ mm^2). During implantation, $BaTiO_3$ crystals were mounted on a 4-in. Si wafer. An Al foil mask allowed the sequential ion implantation with H^+ and He^+ ions. The ion-implantation condition was 80 keV for H^+, with a dose of 5×10^{16}–1×10^{17} cm^{-2} and 115 keV with a dose of 1×10^{17} cm^{-2} for He^+. All implantations were performed at −25 °C. Prior to cavity nucleation and rupture observations, the isochronal annealing was performed in a high-vacuum ($<1\times10^{-6}$ torr) rapid thermal annealing (HV-RTA) chamber from 300 to 600 °C.

The surface energy of the $BaTiO_3$ single crystal following the H^+/He^+ implantation was measured by contact angle measurements, using water and di-iodomethane droplets with a constant droplet volume of 20 dm^3 using a double laser-beam goniometer. At room temperature, the surface energy is 61.1 mJ/m^2 and for the temperature-dependent surface energy, we used the phenomenological equation $\gamma(T)=6.11\times10^{-2}+3.82\times10^{-5}T$ from assuming the $\gamma_o(1+T/T_o)$, where T_o is the critical temperature at which the solid-gas interface is vanishing.[18]

Polarized optical microscopy (OM), contact mode atomic force microscopy (AFM), and focused-ion-beam scanning electron microscopy (FIB-SEM) were used to image the cavity geometry and distribution. Nanomechanical characterization of an annealed $BaTiO_3$ sample was performed using a nanoindentation system (Hysitron Triboscope) in conjunction with AFM (Veeco Dimension 3100 AFM). Nanoindentations for material property characterization were performed using a three-sided Berkovich diamond indenter. Bending tests were performed on blisters using a conical diamond indenter with a 1-μm tip radius. A ramping load was applied to the center of a cavity, while force and displacement data were recorded. Prior to testing, each cavity specimen was imaged *in situ* using a diamond conical tip to determine its shape and diameter.

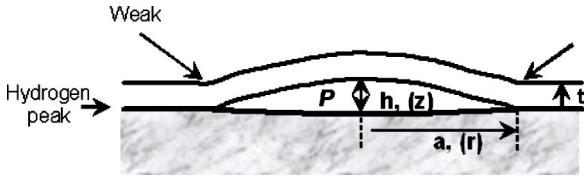

FIG. 1. Schematic diagram of the cavity geometry with hydrogen implantation, with the ion projected range (R_p) indicated by the hydrogen peak; t is the blistered film thickness (i.e., part removed from the bulk crystal), p is the internal pressure, h is the height of the cavity, and r is the radius.

III. THEORY FOR CAVITY FORMATION

After ion implantation in the ion-implanted layer, the implanted atoms reside in the crystal lattice at a depth near the ion projected range and could conceivably combine with one of the elements in the $BaTiO_3$ lattice, forming X–H or X–OH complexes (where X is Ba or Ti). During subsequent thermal annealing, the trapped hydrogen and He atoms diffuse out and segregate near the peak of the implanted gas concentration profile, forming microcavities filled with H_2 and He molecules. The pressure inside the cavity will act as the driving force for its growth and expansion at the initial stage of annealing.[19] In Fig. 1, the schematic diagram of cavity nucleation and growth from the certain depth range with ion implantation is shown. According to fracture mechanics and the thermodynamic nucleation theory, the shape and size of the cavity with the number of gas molecules at a given temperature are determined by the surface energy and the elastic parameters of $BaTiO_3$.[20] The z component of the surface displacement is

$$u_z = \pm a\frac{p}{E}\frac{4(1-\upsilon^2)}{\pi}\sqrt{1-\frac{r^2}{a^2}}, \tag{1}$$

where a is the radius of a cavity, r is the radius at $z=0$, p is the hydrogen gas pressure which is dependent on geometric factors of the growing cavity, such as the cavity radius and height, E is Young's modulus, and υ is Poisson's ratio. This equation indicates the effect of the volumetric expansion of the cavity, resulting from the hydrogen gas pressure and the elastic parameters of the host material.

Figure 2 shows the stopping and range profile for implanted species obtained via the Monte Carlo ion trajectory (SRIM 2003) simulation results for H^+ and He^+ ions, respectively.[21] According to the SRIM simulation, the ion-implantation conditions employed (80 keV for H^+ with a dose of 5×10^{16}–1×10^{17} cm^{-2} and 115 keV with a dose of 1×10^{17} cm^{-2} for He^+) gave rise to a projected ion distribution peak depth R_p and a straggle range ΔR_p of 449.3 and 80.9 nm for H^+ ions, respectively, and 432.5 and 111.2 nm

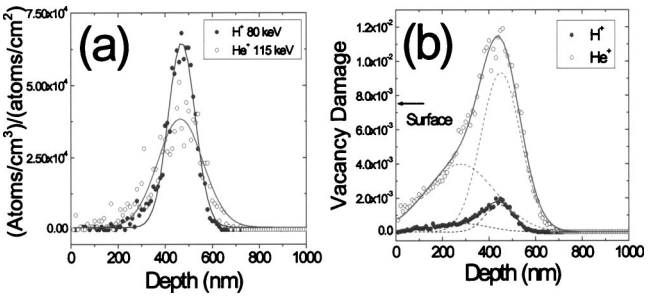

FIG. 2. SRIM simulation results for H^+ and He^+ ion implantation. (a) Ion depth profile and (b) vacancy damage formation from ion collision for H^+ (80 keV) and He^+ (115 keV) ions. The data obtained from SRIM Monte Carlo simulations are fitted by Gaussian profiles to show the distribution of ions and vacancy defects.

for He^+ ions, respectively. The He^+ ion implantation yields a larger straggle than does the H^+ implantation. Furthermore, a higher concentration of ion-induced vacancies is produced by He^+ implantation. We speculate that these additional defects from the He implantation and the wider ion distribution may accelerate cavity nucleation during the subsequent anneal. The effect of H^+ and He^+ ion co-implantation on cavity nucleation will be discussed elsewhere.

IV. RESULTS

A. Thermodynamics of cavity nucleation

Figure 3(a) shows typical images for the cavity distribution and geometry after isochronal annealing observed by optical microscopy. Figure 3(b) shows AFM images after the cavity ruptures. The ruptured cavity depths (400–500 nm) are consistent with the values that are expected in the SRIM simulation.

The driving force for lateral cavity propagation is the internal cavity pressure, which is caused by the hydrogen gas trapped in the cavity after diffusion from the surrounding implanted region.[22] The governing equation for excess pressure in a cavity, relative to ambient pressure, can be written as

$$\Delta p = \frac{64hEt^3}{12r^4(1-\nu^2)}, \tag{2}$$

where E is Young's modulus for $BaTiO_3$, t is the thickness of the blistered film, h is the height of the cavity, and ν is Poisson's ratio and is equal to 0.3. Thus, one can obtain an

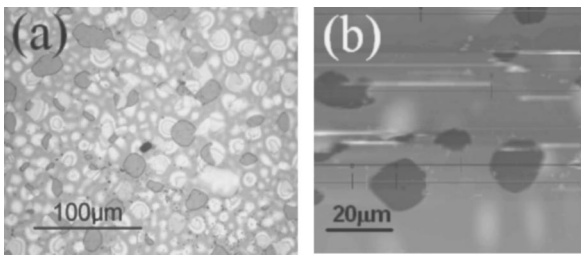

FIG. 3. (a) Optical microscope image illustrating cavity distribution and blistering, (b) large-area AFM scan. Average crater depth after the partial blistering is 452 nm, which is consistent with the SRIM simulation result. Hydrogen ions were implanted with a dose of 1×10^{17} cm^{-2}. The annealing was performed at 300 °C for 30 min.

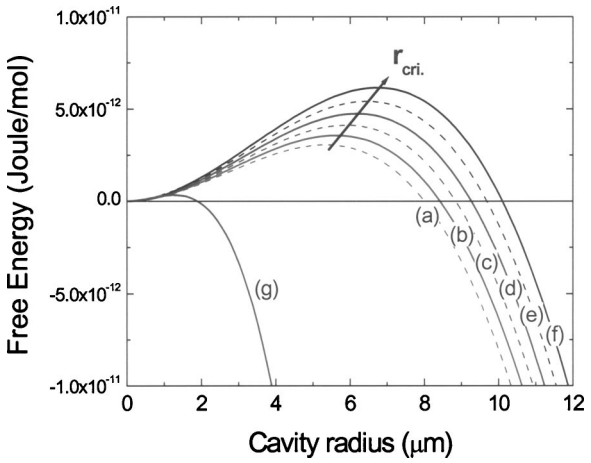

FIG. 4. Total Gibbs free energy of a growing cavity in $BaTiO_3$ as a function of temperature derived from Eq. (4) and the Young's modulus (120 GPa) of $BaTiO_3$, measured using nanoindentation at (a) 300, (b) 400, (c) 500, (d) 600, (e) 700, and (f) 800 °C, and a (g) similar data for Si at 500 °C from Ref. 18.

expression for the pressure difference Δp in terms of r and h.[23] From AFM measurements, we obtained the cavity geometry (r and h), and the inner cavity pressure is in the range $4\ \text{MPa} < \Delta p < 500\ \text{MPa}$.

The shape of the nucleated cavity that can result in a second phase is determined by the strain energy of the solid, the surface energy, and the free energy of the molecules. The strain energy **U** of bulk $BaTiO_3$ around the cavity, the crack surface energy **E**, and the external potential energy **P** can be determined[18] and thus the total free energy of a growing cavity can be written as

$$\Delta G(r,T) = U(r) + E(r) + P(r,T), \tag{3}$$

$$\Delta G = \frac{16p^2(1-\nu^2)}{\pi E}r^3 + 2\pi\gamma r^2 - \frac{16p^2(1-\nu^2)}{3E}r^3. \tag{4}$$

At the condition for cavity nucleation, $dG(r,T)/dr=0$, one can obtain the critical radius as

$$r_{\text{critical}} = \frac{\pi\gamma(T)E}{0.18p^2(1-\nu^2)}. \tag{5}$$

In Fig. 4, the Gibbs free energy and the critical radius for each temperature are shown. The free energy for cavity nucleation becomes maximal at the critical radius, whereas in the regime where the radius is smaller than the critical radius, dG/dr is larger than zero. Here, the cavity is unstable and shrinks away if an additional driving force is not present. For a cavity radius larger than the critical radius, a cavity grows indefinitely or until the cavity ruptures or coalescence with another cavity intervenes. Because of the differences of elastic properties and surface energy, which are terms for volume and surface contributions on a cavity nucleation, Si has a smaller critical cavity radius (1–1.5 μm at 500 °C) than that for $BaTiO_3$.

Hydrogen-induced cavity rupture is a chemical as well as a physical process, whereas He^+ co-implantation is an inert ambient in the damaged zone and it makes more interstitial and vacancy defects as shown in the SRIM results [Fig.

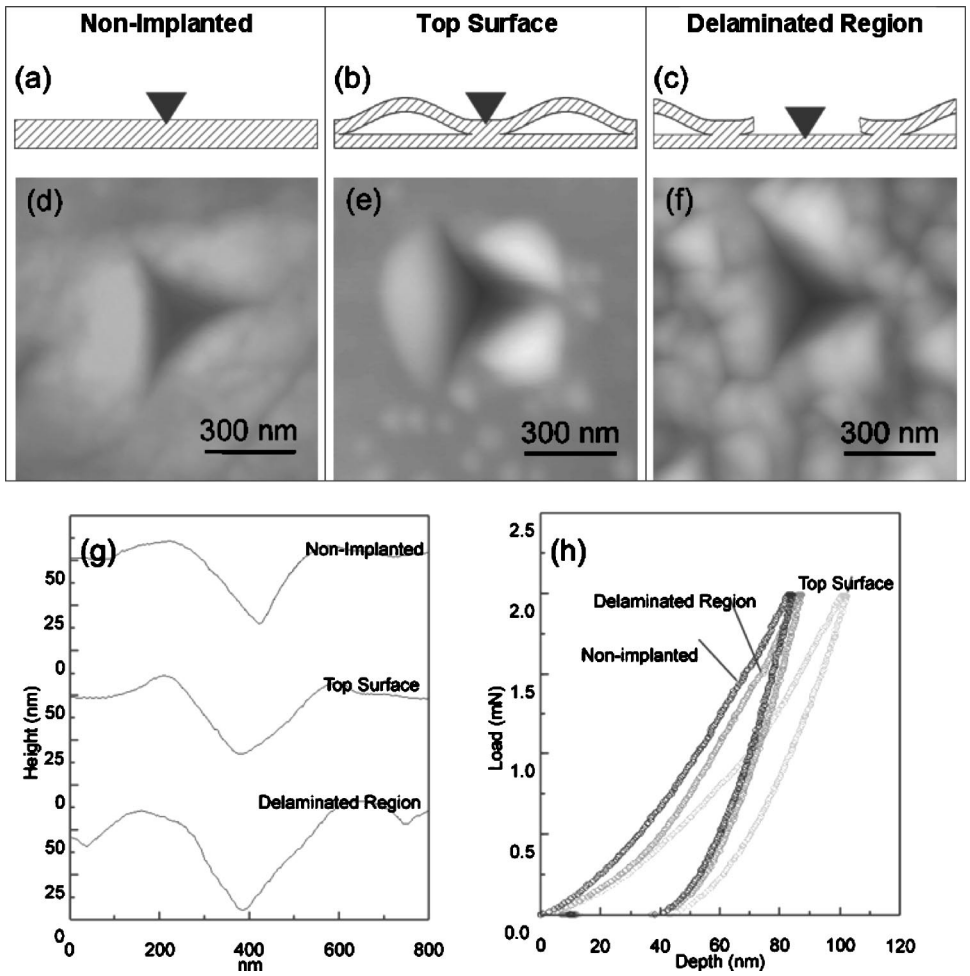

FIG. 5. Nanoindentation tests performed on unimplanted bulk $BaTiO_3$ [(a) and (d)], hydrogen-implanted $BaTiO_3$ sample at the top surface [(b) and (e)] and in delaminated regions [(c) and (f)]. AFM images [(d)–(f)] and cross-sectional views (g) show the indentation marks made with a Berkovich indenter tip. Analysis of the collected load/displacement curves (h) showed that the unimplanted bulk $BaTiO_3$ has the highest elastic modulus and hardness, followed by the implanted $BaTiO_3$ sample, and the delaminated region. The implanted sample (H^+ ion dose $= 1 \times 10^{17}$ cm^{-2}) was annealed at 500 °C for 30 min.

2(b)]. The vacancy defects in the implanted area is mainly from He (89.5% of the total vacancy damage). This high-vacancy damage near the peak ion-projection range enables cavity rupture at a stage earlier than is predicted by thermodynamic modeling alone.

B. Nanoscale mechanical testing

Nanoindentation tests were performed on unimplanted bulk and hydrogen-implanted/annealed $BaTiO_3$ samples, as shown in Fig. 5. The Young's modulus and hardness of the bulk $BaTiO_3$ single crystal are 182.12 ± 14.24 GPa and 12.40 ± 0.95 GPa, respectively. The hydrogen-implanted sample reveals a marked decrease in Young's modulus and hardness. An examination of the top surface in areas where hydrogen cavities have not formed [as in Fig. 5(b)] resulted in a measured local modulus of 120.3 ± 4.8 GPa and a hardness of 10.7 ± 0.8 GPa. Thus hydrogen implantation decreased the Young's modulus and hardness of $BaTiO_3$. The delaminated regions, areas where the cavity pressure caused layer exfoliation (rupture and separation) of the film on top of a cavity [Fig. 5(c)] exhibit a Youngs' modulus of 166 ± 17.6 GPa and a hardness of 10.1 ± 2.6 GPa, which are close to the values of bulk $BaTiO_3$. The measured delaminated region depth is approximately 450 nm, which is in good agreement with the SRIM results. This indicates that the hydrogen implantation changes the mechanical properties only within the ion-projected depth range.

The bending tests for individual cavities also reflect the mechanical property changes. The bending tests on the cavities such as the one shown in Fig. 6(a), resulted in an initial linear response, a slight increase in stiffness due to the rising cavity pressure from the decreasing volume, and a final sharp increase in stiffness corresponding to the contact of the upper and lower cavity surfaces at the center. The initial stiffness was collected from the linear portion of the different loading tests, and Fig. 6(b) compares the experimental results with predictions generated using finite element (FE) analysis. The FE models used the average depth value measured by AFM and assumed a Poisson's ratio of 0.3 for the material. As expected, the pressure inside the cavity was found to have a negligible effect on the plate stiffness. Calculated at a range of diameters and elastic moduli, the FE results suggest an effective modulus of just below 120 GPa, roughly the same value measured at the top surface.

The decreased modulus and hardness values are attributed to the crystal lattice parameter changes, defect generation, and phase transformation caused by hydrogen ion implantation. As illustrated in Fig. 1, implantation injects hydrogen ions into the crystalline $BaTiO_3$ matrix, thereby deforming the crystal lattice and generating defects such as vacancies. Thermal annealing causes diffusion and coalescence of the atoms in cavity nucleation, and after annealing at 600 °C residual hydrogen cannot be detected by elastic-recoil spectrometry ion-scattering methods, while lattice

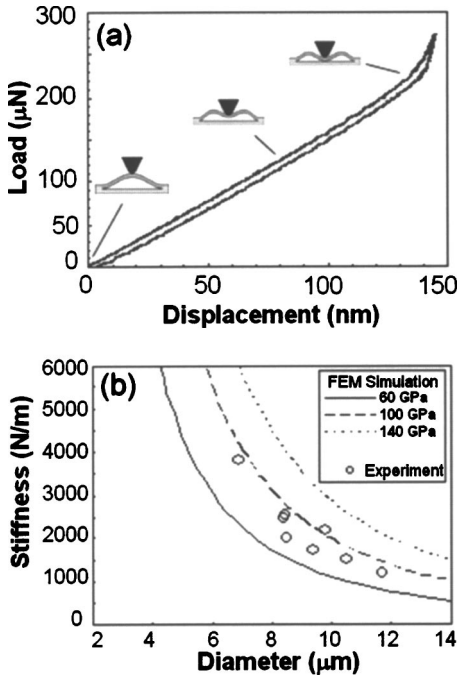

FIG. 6. Bending tests performed with a point load source at the center of blisters. An individual loading curve (a) shows an initial region of linear response, a region of gradually increasing stiffness due to increasing cavity pressure, and a sharp increase in stiffness at the point of cavity collapse. (b) Comparison of a number of blister stiffnesses, measured from the initial linear region of the loading curves, with finite element (FE) analysis predicting an elastic modulus of slightly less than 120 GPa for the $BaTiO_3$ material.

damages are partially recovered to the original crystal state as confirmed by Raman spectroscopy and transmission electron microscopy (TEM).[14] The annealed material cannot be recovered to the original crystal state. The crystal lattice changes, defect generation, and phase transformation in the annealed layered are believed to contribute to the lower Young's modulus and hardness. This is further supported by the fact that delamination and cavity rupture occurred at the thickness which corresponds to the expected peak concentration of hydrogen ions, as shown in Fig. 1.

Based on the experimental results obtained from nanoindentation, we performed FE calculations for a single cavity with a diameter of 8.5 μm, which corresponds to the critical radius obtained in the experiment, as shown in Fig. 7. The results of the FE analysis of cavity pressure show high levels of strain, reaching 1.05% at the outer ring of the vesicles [Fig. 7(d)]. We note that in this highly strained region, the local strains would be high enough to enable a ferroelectric phase transition or 90° domain switching of a *c-a* domain if annealed below the Curie temperature. In $BaTiO_3$, for example, 90° domains were shown to be nucleated by a compressive stress of 0.22 MPa and the removal of the 90° domains was initiated at a stress above 1.1 MPa.[24] As cavity growth proceeds, nearly all of the material in the vicinity of the ruptured cavity will be exposed to these high strains and deformations.

V. DISCUSSION

In the previous sections, we developed thermodynamic arguments for the feasibility of cavity nucleation and growth and the observed mechanical property changes after high-energy and high-dose ion implantation and cavity growth. We now combine these results to propose a strain-induced layer exfoliation mechanism.

First, we showed the feasibility of bubble nucleation and growth, with hydrogen and helium gases residing in the $BaTiO_3$ lattice. In this gas-solid phase system, one possible mechanism of cavity nucleation and layer exfoliation may be pressure-induced thermal creep because there is a considerable pressure exerted on the layer by the gas-containing cavity during annealing. The gas-filled cavities are pressurized and the release of gas molecules from the cavity does not occur until it meets another neighboring cavity upon coalescence or during large-area exfoliation. It is possible that the gas released from a cavity can also occur via an Ostwald-ripening mechanism, although this probably plays a small role during large-area exfoliation.[22] In the final stage of gas release (cavity rupture and layer splitting) during annealing, the cavity radius (volume) might be increased by purely thermal creep. The other driving force for cavity growth, as shown in Sec. IV B, is the reduction of elastic strain energy. Once the cavity expansion proceeds beyond the critical ra-

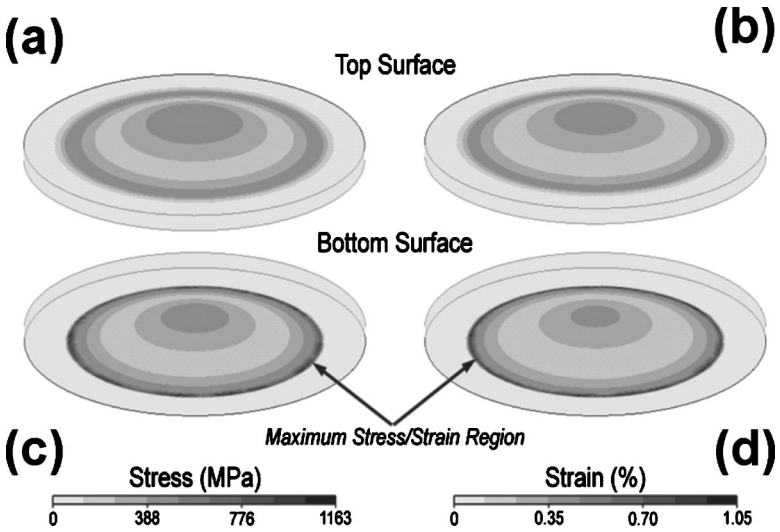

FIG. 7. Simulation results using finite element (FE) method for the strain [(a) and (c)] and strain [(b) and (d)] distributions with pressure loading of a single blister bubble. The results show a ring-shaped region of high stress/strain concentrations on the bottom surface of the cavity that forms the crack tip of the hydrogen cavity.

dius, it is a spontaneous process and the cavity expands to minimize the free energy of the system, as shown in Sec. IV A.

VI. CONCLUSION

We have developed a thermodynamic model for cavity nucleation and growth in $BaTiO_3$, following high energy and dose ion implantation. The nanomechanical property changes in local regions on, near, and away from developed cavities were investigated by nanoindentation. The critical radius of the cavity nucleation and spontaneous growth has been estimated from classical nucleation theory. During cavity nucleation, the thermaleffusion of hydrogen from the $BaTiO_3$ lattice and interstitial vacancies is the kinetically limiting mechanism for lateral cavity growth. The gas pressure within a cavity is the major driving force for cavity opening and layer exfoliation. The present analysis of cavity nucleation and growth and the corresponding local mechanical properties of the $BaTiO_3$ crystal surveys the mechanisms for layer exfoliation and can be used to guide and optimize the process conditions for ion-implantation-induced layer transfer of high-quality $BaTiO_3$ single-crystal thin films.

ACKNOWLEDGMENTS

This work has been supported by the Army Research Office (ARO-MURI) under Grant No. DAAD 19-01-1-0517, Arrowhead Research Corporation, and the National Science Foundation (Grant No. EPS-0296165), the University of South Carolina NanoCenter Seed Grant, and the South Carolina Space Grant Consortium-NASA. One of the authors (Y.-B. Park) wishes to acknowledge the support of the postdoctoral fellowship program from the Korea Science and Engineering Foundation (KOSEF).

[1] F. Jona and G. Shirane, *Ferroelectric Crystals* (Dover, New York, 1962).
[2] A. I. Kingon, J. P. Maria, and S. K. Streiffer, Nature (London) **406**, 1032 (2000).
[3] D. L. Polla and L. F. Francis, Annu. Rev. Mater. Sci. **28**, 563 (1998).
[4] M. Bruel, Electron. Lett. **31**, 1201 (1995).
[5] Q. Y. Tong, K. Gutjahr, S. Hopfe, U. Goesele, and T. H. Lee, Appl. Phys. Lett. **70**, 1390 (1997).
[6] James M. Zahler, C. G. Ahn, S. Zaghi, H. A. Atwater, C. Chu, and P. Iles, Thin Solid Films, **403–404**, 558 (2002).
[7] L. B. Freund, Appl. Phys. Lett. **70**, 3519 (1997).
[8] M. Levy, R. M. Osgood, R. Liu, L. E. Cross, G. S. Cargill, A. Kumer, and H. Bakhru, Appl. Phys. Lett. **73**, 2293 (1998).
[9] L. J. Huang, Q. Y. Tong, and U. Gosele, Electrochem. Solid-State Lett. **2**, 238 (1999).
[10] T. Izuhara, I. Gheorma, R. M. Osgood, A. N. Roy, H. Bakhru, Y. M. Tesfu, and M. E. Reeves, Appl. Phys. Lett. **82**, 616 (2003).
[11] F. J. Kub, K. D. Hobart, J. M. Pond, and S. W. Kirchoefer, Electron. Lett. **35**, 477 (1999).
[12] M. Levy, R. M. Osgood, A. S. Bhalla, R. Guo, L. E. Cross, A. Kumar, S. Sankaran, and H. Bakhru, Appl. Phys. Lett. **77**, 2124 (2000).
[13] I. Szafraniak, I. Radu, R. Scholz, M. Alexe, and U. Gosele, Integr. Ferroelectr. **55**, 983 (2003).
[14] Y.-B. Park, J. L. Ruglovsky, and H. A. Atwater, Appl. Phys. Lett. **85**, 455 (2004).
[15] B. Bhushan and X. Li, Int. Mater. Rev. **48**, 125 (2003).
[16] X. Li and B. Bhushan, Mater. Charact. **48**, 11 (2002).
[17] X. Li and B. Bhushan, J. Mater. Res. **14**, 2328 (1999).
[18] W. Han and J. Yu, J. Appl. Phys. **89**, 6551 (2001).
[19] C. M. Varma, Appl. Phys. Lett. **71**, 3119 (1997).
[20] F. Yang, J. Appl. Phys. **94**, 1454 (2003).
[21] J. F. Ziegler, J. P. Biersack, and U. Littmark, *The Stopping and Range of Ions in Solids* (Pergamon, New York, 1985).
[22] M. Weldon *et al.*, J. Vac. Sci. Technol. B **15**, 1065 (1997).
[23] L. J. Hunag, Q. Y. Tong, Y. L. Chao, T. H. Lee, T. Martini, and U. Gosele, Appl. Phys. Lett. **74**, 982 (1999).
[24] Z. Li, C. M. Foster, X.-H. Dai, X.-Z. Xu, S.-K. Chan, and D. J. Lam, J. Appl. Phys. **71**, 4481, (1992).